AIAA JOURNAL
Vol. 38, No. 5, May 2000

Numerical Simulation of a Three-Dimensional Flame/Shock Wave Interaction

Christopher J. Roy* and Jack R. Edwards†
North Carolina State University, Raleigh, North Carolina 27695-7910

A three-dimensional Navier–Stokes solver for chemically reacting flows is used to study the structure of a supersonic hydrogen-air flame stabilized in a Mach 2.4 rectangular cross-section wind tunnel. The numerical model uses a 9-species, 21-reaction hydrogen oxidation mechanism and employs Menter's hybrid k-ω/k-ε turbulence model. An assumed probability density function is used to account for the effects of turbulent temperature fluctuations on the ensemble-averaged chemical reaction rates. Results are presented for a configuration studied at the University of Michigan in which the effects of wedge-generated shock waves on flame stability were determined. Computed pitot and static pressure profiles are compared with experimental measurements, and axial density gradient contour plots are compared with experimental schlieren photographs. The highly three-dimensional structure of the flame is described in detail, and stabilization mechanisms are discussed.

Introduction

HYPERSONIC vehicles will play an important role in air and space transportation in the 21st century. Current orbital launch vehicles rely primarily on rocket engines, which suffer from the need to store both fuel and oxidizer, with the latter generally comprising up to 65% of the vehicle's takeoff weight,[1] thereby greatly decreasing payload capacity. Airbreathing vehicles, on the other hand, have the potential for larger relative payload capacities because they use external air as the oxidizer in the combustion process. In addition, airbreathing vehicles can be designed to employ horizontal landing and/or takeoff, resulting in much faster mission turnaround times.

Ramjets are often used for supersonic flight speeds below Mach 5. In these devices, the airstream is slowed down to subsonic speeds before entering the combustor. Above Mach 5, the high static temperatures generated by the compression process cause the air to dissociate into atomic nitrogen and oxygen, with a significant amount of the flow energy used to break the molecular bonds. At such high Mach numbers it is thus necessary to employ a supersonic combusting ramjet (scramjet), where combustion takes place in the supersonic regime. Scramjets contain a number of complex flow features, including shock waves, expansion fans, boundary layers, shear layers, compressible turbulence, reaction fronts, and regions of both supersonic and subsonic flow. The understanding of the interactions among these features is a key in the development of viable scramjet engines.

Experimental data on supersonic combustion are scarce because of difficulties in simulating high-enthalpy conditions in ground-based combustion facilities. Vitiated air generated during a precombustion process is often used to simulate the high-enthalpy airflow entering a supersonic combustor. This method leads to the presence of significant amounts of water vapor (a combustion product) in the airstream and to the presence of radical species, both of which may influence flame ignition and stabilization characteristics. It is also difficult to characterize the effects of wave interactions on the combustion process in typical facilities.

Presented as Paper 98-3210 at the AIAA/ASME/SAE/ASEE 34th Joint Propulsion Conference, Cleveland, OH, 13–15 July 1998; received 25 February 1999; revision received 20 August 1999; accepted for publication 20 August 1999.

*Research Assistant, Campus Box 7910, Department of Mechanical and Aerospace Engineering; currently Senior Member of Technical Staff, P.O. Box 5800, Mail Stop 0825, Aerosciences and Compressible Fluid Mechanics Department, Sandia National Laboratories, Albuquerque, NM 87185-0825; cjroy@sandia.gov. Member AIAA.

†Assistant Professor, Campus Box 7910, Department of Mechanical and Aerospace Engineering; jredward@eos.ncsu.edu. Senior Member AIAA.

Computational fluid dynamics (CFD) analyses of scramjet combustors are also difficult for a variety of reasons. The effects of compressibility on the turbulence are not well understood, and adequate models for the effects of turbulent fluctuations on reaction rates remain to be found. Standard fast chemistry assumptions are no longer valid, as residence times may be short enough such that finite-rate effects become important. Thus, reasonably detailed chemical reaction mechanisms and a large number of chemical species may be required, particularly to simulate ignition and stabilization effects. The disparity in characteristic timescales for convective, acoustic, diffusive, and reactive phenomena can cause severe time-step limitations, and the need to account for interactions among the flow features just mentioned requires the use of reasonably fine computational meshes.

Three-dimensional numerical studies of scramjet combustors have focused on fuel-injection methods that enhance fuel-air mixing while minimizing total pressure losses in the combustor. Computational results have been presented by Eklund and Stouffer[2] using a two-zone algebraic turbulence model and finite-rate chemistry; however, turbulence-chemistry interactions were neglected. Baurle et al.[3,4] presented results for this same configuration using the Wilcox k-ω turbulence model and finite-rate chemistry. These calculations used assumed-shape probability density function (PDF) closures to account for the effects of turbulent fluctuations in temperature and composition. Recently, Baurle et al.[5] performed three-dimensional computations on an ethylene scramjet combustor using a recessed cavity flameholder. The two-equation Menter shear-stress transport turbulence model[6] was used along with reduced chemistry mechanisms for ethylene oxidation. Because of the approximate nature of the chemistry model, the effects of turbulence-chemistry interactions were not included.

Recently, Driscoll and coworkers at the University of Michigan have developed a scramjet test facility consisting of an axisymmetric hydrogen burner oriented along the centerline of a rectangular cross-section Mach 2.4 wind tunnel. The airstream uses resistively heated air capable of stagnation temperatures near 1100 K, which overcomes some of the problems present in vitiated air experiments. This group has examined both flame length[7] and blowout stability limits[8] for a number of supersonic hydrogen flames. Heat-release patterns, pressure losses, and thermal choking limits were also reported by Yoon et al.[9]

Huh and Driscoll[10,11] found that supersonic flame lengths could be significantly reduced by the addition of wedges to the wind-tunnel side walls. It was theorized that the wedges created radial inflow of air into the flame, thus enhancing turbulent mixing of the fuel and air. However, later studies[12,13] suggested that the reduced flame lengths were a consequence of incomplete combustion of the fuel. The possible importance of baroclinic torque mechanisms[2,14,15] as a means

of mixing enhancement was also investigated,[10,11] but results were inconclusive. In all cases the presence of the wedges improved flame stability. The database of Huh and Driscoll includes measurements of pitot and static pressures within the combustor as well as schlieren photographs of the flame structure.

A difficulty in using the Huh and Driscoll database for CFD validation purposes is that the static temperatures in the wind tunnel are significantly lower than that anticipated in actual scramjet engines, ranging from values of around 150 K for a stagnation temperature of 294 K to values of around 600 K for the maximum attainable stagnation temperature of 1100 K, with the majority of quantitative data at the lower temperature. These values are well below the autoignition temperature of hydrogen, meaning that the process of numerical flame stabilization becomes much more difficult. To the authors' knowledge, the experiments of Huh and Driscoll[10,11] have not previously been studied with computational methods. The present work describes an attempt to simulate some of these experiments using a three-dimensional Navier–Stokes solver that has been previously validated for high-speed reactive flows.[16] Results are presented for a shock/flame interaction and a case without combustion, both in comparison with the data of Refs. 10 and 11. A discussion of the structure of these highly three-dimensional flowfields concludes this article.

Flowfield Model

The reacting flowfields considered here are assumed to be governed by the three-dimensional Favre-averaged Navier–Stokes equations, formulated in a generalized coordinate system and expanded to include separate transport equations for each important molecular constituent. The thermodynamic state of the gas mixture is defined by the constraint that the sum of the mass fractions ($Y_k = \rho_k/\rho$) equal unity, the state equation

$$p = \sum_k p_k = \sum_k \rho_k \frac{\mathcal{R}_u}{W_k} T$$

expressions for the enthalpy of each molecular constituent

$$h_k = h^0_{f,k} + \int_{T\,\mathrm{ref}}^{T} C_{p,k}(T)\,\mathrm{d}T$$

and a relation for the mixture enthalpy:

$$\rho h = \sum_k \rho_k h_k$$

In the preceding expressions W_k is the molecular weight of species k, ρ_k is the species density, $\mathcal{R}_u$ is the universal gas constant, $h^0_{f,k}$ is the enthalpy of formation of species k, and $C_{p,k}$ is the specific heat at constant pressure of species k. Curve-fit polynomials for the variation of $C_{p,k}$ with temperature are obtained from McBride et al.[17] Expressions for species molecular viscosity and thermal conductivity are also obtained from Ref. 17, with Wilke's law used to determine mixture values. Molecular diffusion velocities are modeled using Fick's law. One diffusion coefficient, related to the mixture viscosity and density via the assumption of a constant Schmidt number, is used for all species. Standard Boussinesq/gradient diffusion approaches are adopted for turbulence closure, reducing the problem to the specification of the eddy viscosity and turbulent Prandtl and Schmidt numbers, both set to 0.7 in this work.

Turbulence closure is provided through Menter's hybrid k-ω/ k-ε model.[6] This model uses distance-dependent blending functions to facilitate a switch from a k-ω formulation near solid surfaces to a k-ε formulation away from solid surfaces and in free shear layers. This treatment eliminates the strong sensitivity of the k-ω model to the specification of ω in the freestream, while preserving its favorable characteristics in the prediction of wall-bounded flows. Turbulence-chemistry interactions are modeled through a simple assumed PDF approach,[18–20] which accounts for the effects of temperature fluctuations on the chemical species production rates. The temperature PDF is a clipped Gaussian distribution that requires the specification of the mean temperature and its variance. A transport equation for the enthalpy variance $\widetilde{h''^2}$ is solved,[20] and the temperature variance is then found by neglecting the effects of temperature fluctuations on the specific heat, i.e.,

$$\widetilde{T''^2} = \widetilde{h''^2} \Big/ \widetilde{C}_p^2$$

To implement the procedure, a table containing the forward and backward reaction-rate coefficients integrated over a suitable mean and fluctuating temperature range is created a priori. Averaged values for the reaction-rate coefficients at a particular mesh point are determined through interpolation of the table entries given mean and variance information extracted from the flow solver. This closure assumes statistical independence among fluctuations in temperature, density, and composition. Moreover, the effects of density and composition fluctuations are omitted from the model entirely. In spite of its theoretical limitations, simple closures of this type have provided reasonable agreement with experimental data for high-speed hydrogen jet diffusion flames, generally tending to promote more rapid ignition.[19,21]

A 9-species, 21-reaction hydrogen-oxidation scheme[22] is used for all calculations, with source terms describing the production or depletion of each species defined by the law of mass action. This mechanism includes chain-initiation and chain-branching reactions involving HO_2 and H_2O_2 as well as the major constituents O_2, H_2, H_2O, OH, O, and H. A transport equation for inert nitrogen is also solved.

Numerical Method

The Navier–Stokes equations are formulated in a cell-vertex finite volume manner, with the inviscid components discretized using Edwards' low-diffusion flux-splitting scheme.[23] This hybrid flux-vector/flux-difference splitting method captures shock waves and reaction fronts without numerical oscillations while resolving shear and boundary layers accurately. The upwind scheme is extended to second-order accuracy using slope-limited variable extrapolation techniques.[23] Viscous and diffusion terms are discretized using central differences.

The governing equations (including the turbulence transport and enthalpy variance equations plus boundary conditions) are formulated in a fully implicit fashion and advanced toward a steady-state solution using a planar Gauss–Seidel iteration strategy.[16] In this approach each (approximately) streamwise-normal plane is solved using a generalized minimum residual Krylov subspace method.[24] The calculations employ local time steps, determined from the acoustic eigenvalues in each coordinate direction using standard techniques. The local time steps are scaled by a user-specified Courant–Friedrichs–Lewy (CFL) number, which is initially set to a relatively low value, then allowed to increase as the calculation proceeds. Representative values for the CFL numbers attained are presented in a later section. Grid sequencing is used to obtain better starting solutions for the calculations on the finest mesh and to assess the effects of mesh refinement on the solution. Sixteen equations (9 species conservation, 3 momentum, 1 energy, 2 turbulence transport, 1 enthalpy variance) are solved per mesh point for the reactive case. Eight equations (2 species conservation, 3 momentum, 1 energy, 2 turbulence transport) are solved per mesh point for the nonreacting (mixing only) flow. The planar Gauss–Seidel method provides reasonably rapid convergence, with fewer than 500 fine-grid iterations typically required to obtain a solution. The method is quite stable but is rather time consuming on a per-iteration/grid point basis, computing at a rate of 2.7×10^{-4} s/iteration/grid point on a Cray T-91D for the larger equation set.

The flowfield model and discretization approach described here has been used extensively for calculations of both low- and high-speed turbulent reactive flows.[16,20,21,25–27] Benchmarking studies pertaining to high-speed combustion can be found in Refs. 20 and 25–27, with Refs. 20 and 25 particularly focusing on the calculation of high-speed jet diffusion flames using two-equation turbulence models. Calculations using Menter's hybrid model as applied to an inlet/combustor flow can be found in Ref. 26.

Calculation Details

Geometry

The Huh and Driscoll[10,11] combustor consists of an axisymmetric fuel tube centered in a rectangular cross-section wind tunnel. The upper and lower walls of the tunnel angle 4 deg away from the

Table 1 Reservoir and combustor inflow conditions

Variable	Air	Fuel
T_0, K	294	294
P_0, atm	6.44	——
Mach (mixing)	~2.45	1.03
Mach (combusting)	~2.45	0.28
$\dot{m}$, g/s	——	1.0
Y_{O_2}	0.233	0
Y_{N_2}	0.767	0
Y_{H_2}	0	1.0

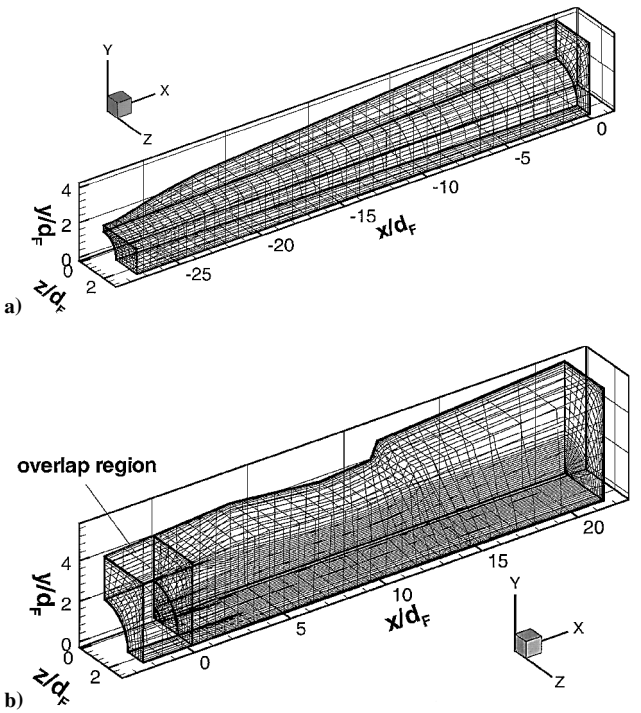

Fig. 1 Grids for the a) inlet (153 × 81 × 49) and b) combustor (129 × 153 × 49), both with every fourth point shown.

center plane to prevent thermal choking, while the sidewalls are straight throughout. Wedges may be mounted on the upper and lower tunnel walls to examine the effects of shock waves on the flow. At the entrance to the combustor, the outer diameter of the fuel tube is 2.54 cm, and the inner diameter (d_F) is 0.7 cm, with the area difference forming an effective bluff body to aid in anchoring the flame. To provide appropriate inflow conditions for the combustor calculation, a separate calculation of the perfect-gas airflow between the wind-tunnel throat and the exit of the fuel tube was performed on a 153 × 81 × 49 mesh (see Fig. 1a). In this calculation and those of the combustor, bilateral symmetry was assumed, meaning that only one-quarter of the flowfield was actually simulated. The combustor grid (129 × 153 × 49) is shown in Fig. 1b. The grid ranges from 2.6 d_F upstream of the fuel tube to 21.4 d_F downstream of the exit plane. Regions within the fuel tube are blanked out of the combustor calculations. Further details of the experimental configuration may be obtained from Refs. 10 and 11. As shown in Fig. 1, the origin is located in the center of the fuel tube at the combustor entrance. The x axis lies in the main flow direction, the z axis is in the direction of the parallel tunnel side wall, and the divergent upper wall lies in the y direction.

Boundary and Initial Conditions

A data plane extracted from the perfect-gas nozzle calculation upstream of the end of the fuel tube was used as the (fixed) inflow plane for the airstream in the simulation of the combustor. Sonic inflow conditions for the nozzle calculation were applied at the nozzle throat corresponding to the reservoir conditions shown in Table 1. Standard no-slip, adiabatic wall boundary conditions were applied on the upper and side walls of the tunnel as well as on the outer surface of the fuel tube. Boundary conditions for the turbulence model were implemented as described in Ref. 6. Values for the axial velocity, thermodynamic variables, and turbulence transport variables along the centerline of the combustor were determined by first extrapolating radial data at each circumferential station to the centerline and then averaging the results. The transverse velocity components on the centerline were set to zero.

The boundary conditions for the fuel jet were initially specified at the choked-flow (sonic) condition corresponding to the measured mass-flow rate of 1 g/s and the fuel jet stagnation temperature of 294 K. Subsequent calculations revealed that the combustor pressure levels were too high to maintain a sonic condition at the fuel tube exit for the reactive cases. As such, the mass-flow rate per unit area, stagnation temperature, flow direction, and composition were specified at the exit plane as per the experiment, and the pressure was extrapolated from the interior. The same boundary condition was applied for the nonreacting cases, as it was unclear a priori whether choked flow could be sustained. This boundary condition resulted in converged fuel jet Mach numbers of 0.28 for the reacting case with shock interaction and 1.03 for the nonreacting case, the latter indicating that choked inflow boundary conditions could have been imposed instead.

The combustor flowfield was initialized by first propagating the air and fuel jet inflow plane properties downstream. Property values behind the fuel tube face were specified as distance-weighed averages of the air and fuel jet properties. To initiate the combustion process, the temperature field behind the fuel tube face was linearly ramped from the already specified values at the $x/d_F = 5.4$ location to 3000 K at the fuel tube face. As the density distribution was held fixed, this temperature ramp also resulted in higher pressures behind the fuel tube, facilitating the rapid formation of the oblique shock system to be discussed later.

Time-Advancement Details

Calculations of the combustor flowfield were started on a 33 × 39 × 13 grid formed by removing every other mesh point twice in succession. Converged first-order accurate results were then interpolated to the next finest mesh (65 × 77 × 25), where second-order converged results were obtained. This solution was interpolated to the finest 129 × 153 × 49 mesh where again second-order solutions were obtained. Initial values for the CFL numbers on each mesh ranged from 0.1 (coarsest mesh) to 5 (finest mesh). The CFL numbers were ramped from these initial values to final values of 15 to 25 as the solution progressed.

Convergence of these complex flowfields was monitored in several ways. L_2 norms of the residual vector, both weighted by the reciprocal of the cell volume and unweighted, were extracted at each iteration. The weighted norm is biased toward smaller cell volumes, characteristic of the viscous layers, whereas the unweighted norm is biased toward the inviscid regions. Maximum residual values were also calculated, and turbulence equation norms were extracted separately. All of these convergence measures tended to level out after a 3.5 to 4 order-of-magnitude residual reduction, measured with respect to the initial values. This required the monitoring of several flow properties to ensure convergence. Pitot pressure and static pressure surveys at locations corresponding with experimental measurements were extracted at each iteration, and computer animations of the data response were produced. Also, the bulk mass-flow rate and elemental hydrogen mass-flow rate at each streamwise station were extracted and monitored at each iteration. The average percent error between the computed mass-flow rate at each station and the inflow mass-flow rate was then determined as another measure of global convergence. Convergence was then assumed when the residual norms settled down to fixed (or slightly oscillatory) values, when the pitot and static pressure distributions changed less than a maximum of 3% (at any point) over 500 iterations and when the percent error in mass-flow rate (either bulk or elemental hydrogen) stabilized to either a fixed or very slowly decreasing value. Final values for the percent errors in elemental hydrogen flow rate were 1.76% for the fine-grid mixing case, 2.65% for the fine-grid

combusting case, 4.43% for the coarse-grid mixing case, and 4.55% for the coarse-grid combusting case. For all cases, final values for the percent error in bulk mass-flow rate were less than 0.5%, the difference indicating that the elemental hydrogen-flow-rate error is more of a measure of the convergence of viscous and diffusive processes, which are typically slower to stabilize.

The fine-grid elemental hydrogen-flow-rate error did exhibit a slow, but consistent decrease with increasing numbers of iterations, and it is possible that further reductions could have been attained. The small anticipated changes in the extracted pressure distributions did not justify the additional expense. The coarse-grid elemental hydrogen-flow-rate errors did not decrease with further iterations after a certain point. This is indicative of calculations on insufficiently refined grids, where the effects of numerical diffusion and general discretization error become more pronounced. In all cases the bulk mass-flow-rate error also did not decrease with further iterations after a certain point. This may be a limitation of the discretization approach, which does not necessarily ensure strict local conservation for complex grid topologies. Although the final levels of error in flow rate are not insignificant, we believe that the calculations are as converged as feasible, given the complexities of both the flowfield and the grid topology, the present discretization method, and the expense of the calculations.

Results

The results of this investigation are presented first through comparisons with available experimental data. A discussion of the flowfield structure for cases with and without combustion concludes this article.

Data Comparisons

The database of Huh and Driscoll[10,11] contains schlieren images, static pressure measurements on the tunnel side walls, and pitot pressure surveys for both reactive and nonreactive cases. Although this database contains results both with and without wedges at various fuel mass-flow rates ($\dot{m}_f$), quantitative comparisons are made for the data with 10-deg wedges at $\dot{m}_f = 1$ g/s, as this configuration is more likely to promote flame stabilization. In addition, Ref. 28 provides planar laser-induced fluorescence (PLIF) measurements of the reaction zone structure, albeit for a configuration without wedges operating at a slightly lower fuel mass-flow rate of 0.95 g/s. Qualitative comparisons with the trends evident from PLIF imaging are presented in the discussion of the flowfield structure.

Schlieren Comparisons

Figure 2a is a contour plot of the axial density gradient at three different constant z planes for the case without combustion. Although no line-of-sight integration was performed, qualitative comparisons can be made with the experimental schlieren photograph shown in Fig. 2b. Both the computations and experiment show an expansion wave (light area) emanating from the fuel-tube outer lip and clearly indicate the location of the free surface dividing the recirculation region behind the bluff body from the airflow (dark line downward from the fuel-tube outer lip). The angle between the free surface and the x axis is less steep in the experimental photograph, indicating that the computation underpredicts the lateral thickness and axial extent of the recirculation zone. Clearly shown is the oblique shock emanating from the 10-deg wedge on the top surface and the transmitted wave originating from the wedge on the lower surface (accounted for in the calculation via symmetry boundary conditions applied at the x-z centerplane). One feature of note in the experimental photograph is an oblique shock wave entering the combustor from the left and traversing the recirculation zone. This feature is not seen in the calculation and is believed to result from a discontinuity in the fuel-tube surface slope evidenced in later sketches of the experimental apparatus,[28] but unfortunately not included in the rendering of the nozzle geometry. With this exception, good qualitative agreement with the experimental results is evidenced.

Figure 3a shows the axial density gradient at constant z planes for the combusting case. Because of viscous layer displacement

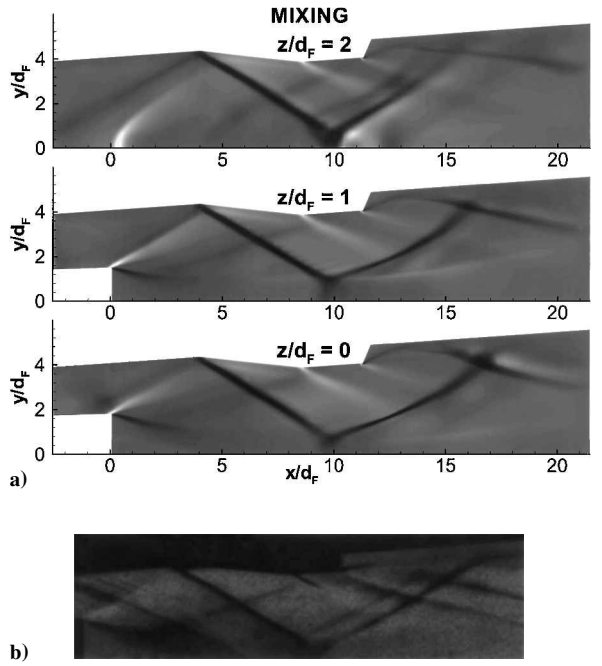

Fig. 2 Mixing case: a) axial density gradient ($\partial\rho/\partial x$) and b) experimental schlieren photograph (reproduced from Ref. 10 with permission from AIAA).

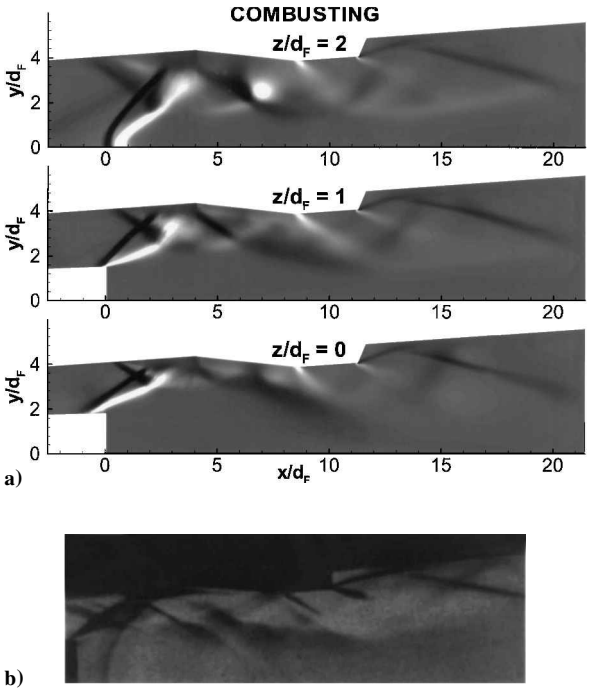

Fig. 3 Combusting case: a) axial density gradient ($\partial\rho/\partial x$) and b) experimental schlieren photograph (reproduced from Ref. 10 with permission from AIAA).

effects discussed later, the leading wave emanating from the tube lip is a shock (dark line), rather than an expansion, as seen in the mixing case. The free surface is now delineated by a white contour (decreasing axial density gradient). In contrast to the nonreacting case, the calculation appears to overpredict the lateral displacement of the recirculation zone when compared with the experimental schlieren presented in Fig. 3b. This overprediction results in a stronger compression of the nominally inviscid wind-tunnel fluid, a stronger expansion as the core fluid spills around the recirculation region, and possibly a more vigorously burning flame. Another consequence is a more severe interaction of the initial shock wave

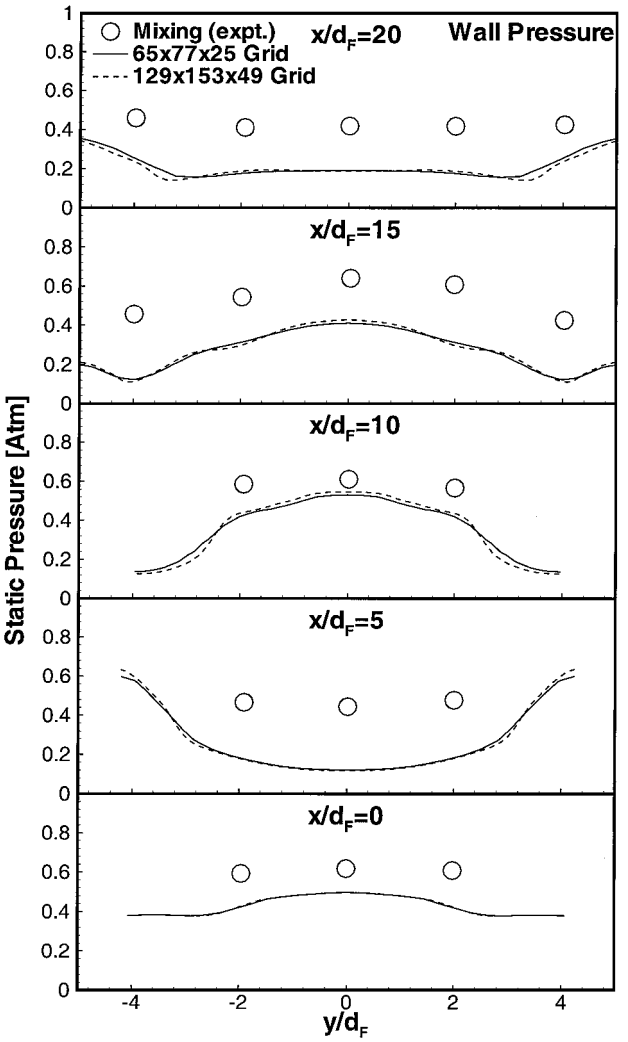

Fig. 4 Wall static pressures on the $z = z_{max}$ side wall for the mixing case with comparison to experimental data of Ref. 10.

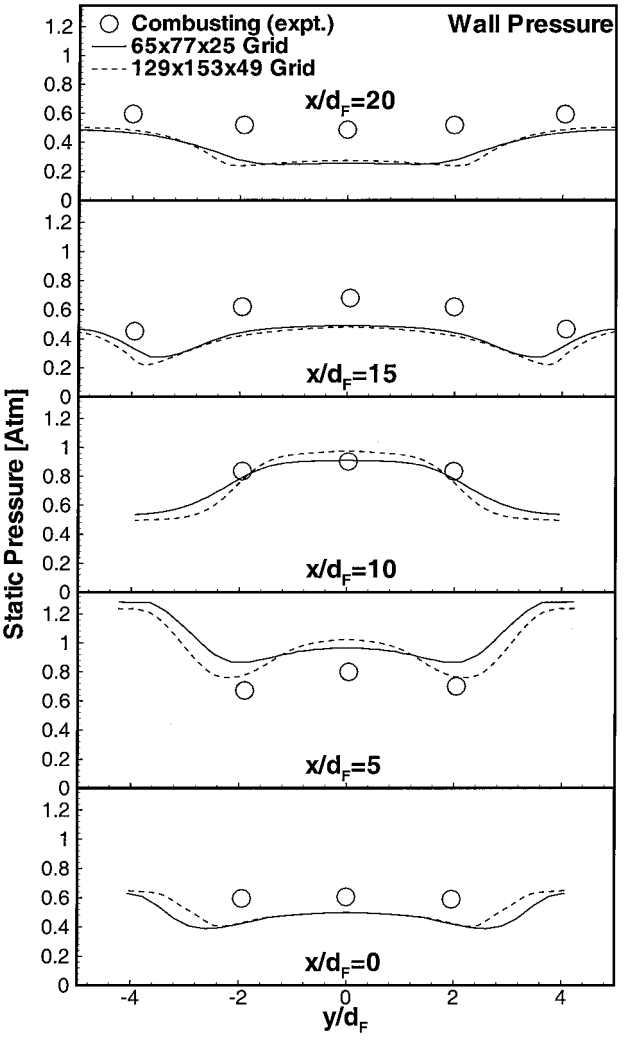

Fig. 5 Wall static pressures on the $z = z_{max}$ side wall for the combusting case with comparison to experimental data of Ref. 10.

with the top wall boundary layer, which results in an overprediction of the size of the separation zone on the upper wall. This strong interaction is manifested in the positioning of the generated separation shock, which is located further upstream in the calculation than in the experiment. Again, good qualitative agreement is evidenced, except for the already mentioned entering wave evident in the schlieren photograph (Fig. 3b).

Surface Pressure Comparisons

Wall static pressures on the tunnel sidewall are presented in Fig. 4 for the mixing case and in Fig. 5 for the combusting case. The pressure distributions for the mixing case follow the trends of the experimental data well but are generally lower in magnitude. This discrepancy can be traced firstly to the inlet flowfield calculation, which results in a generally higher average Mach number at the entrance plane (2.52) than the experiment suggests (2.4). This effect may be a result of the inexact rendering of the fuel-tube surface shape just discussed. The rapid lowering of the pressure level at the $x/d_F = 5$ station is a consequence of the underprediction of the size of the recirculation zone and the resulting overexpansion of the inviscid core fluid. This underprediction is consistent with results for subsonic axisymmetric bluff-body stabilized flames[21,29] using the standard k-ε turbulence model, to which Menter's hybrid model reduces in this region of the flow. Pressure distributions obtained on the coarser $65 \times 77 \times 25$ grid are only slightly different from the fine-grid results.

Results from the reactive case (Fig. 5) also follow the trends of the experimental data quite well. Pressure levels higher than the experimental values are observed at the $x/d_F = 5$ station, a result of the overprediction of the lateral extent of the recirculation zone also noted in the schlieren comparisons. This overcompression is followed by a stronger expansion than observed in the experiment, resulting in lower pressure levels at the downstream stations. The effects of mesh refinement are only significant at the $x/d_F = 5$ station.

Pitot Pressure Comparisons

Computed pitot pressure distributions along the tunnel centerline ($z/d_F = 0$) and the midplane ($z/d_F = 1.45$) are shown in Figs. 6–9 for cases with and without combustion. The mixing results (Figs. 6 and 7) agree reasonably well with the rather sparse experimental data except at the $x/d_F = 5$, $z/d_F = 1.45$ station, where the calculation predicts a higher pitot-pressure level at the centerline. This again is a result of the underprediction of the size of the recirculation zone—the calculation indicates that this profile is in the faster-moving inviscid core flow rather than in the recirculation zone. Results from the combusting case (Figs. 8 and 9) are also in good agreement with the experimental pitot-pressure distributions, which display some deviations from bilateral symmetry. The effects of grid refinement on the predictions are again minimal.

Flow Structure: Reacting Case

Although some discrepancies are present, the level of agreement evidenced in the data comparisons just discussed lends support to the use of the computational results in describing the detailed structure of the reacting and nonreacting flowfields. The three-dimensional structure of the fine-grid combusting case is highlighted in Figs. 10a–10c and Figs. 11a, 11c, and 11d. Key features of the flowfield are referenced in the discussion by capital letters A–T

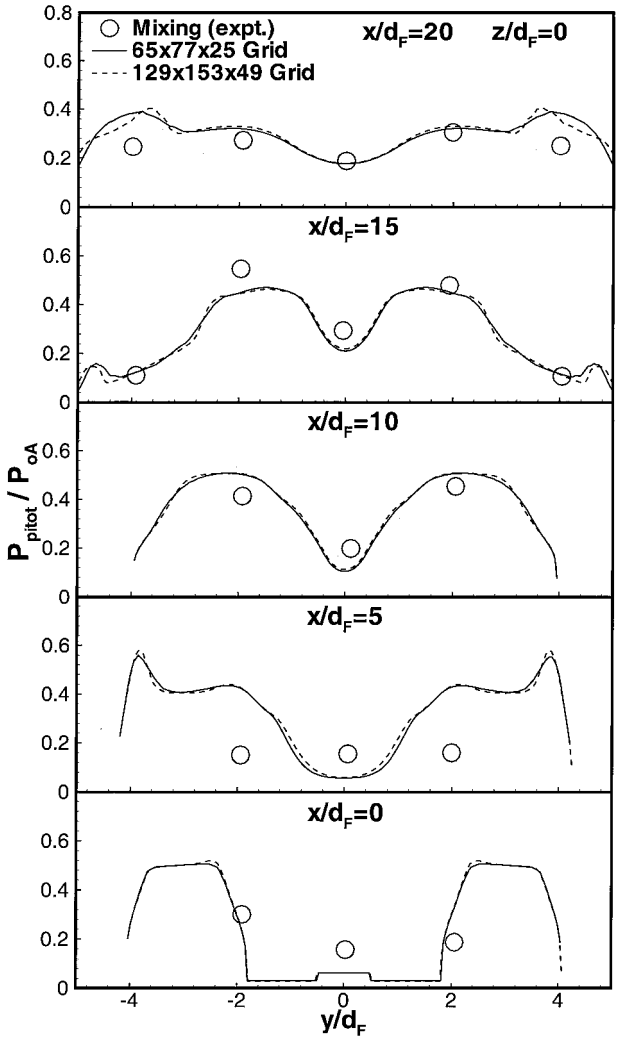

Fig. 6 Normalized pitot pressures at the $z/d_F = 0$ centerplane for the mixing case with comparison to experimental data of Ref. 10.

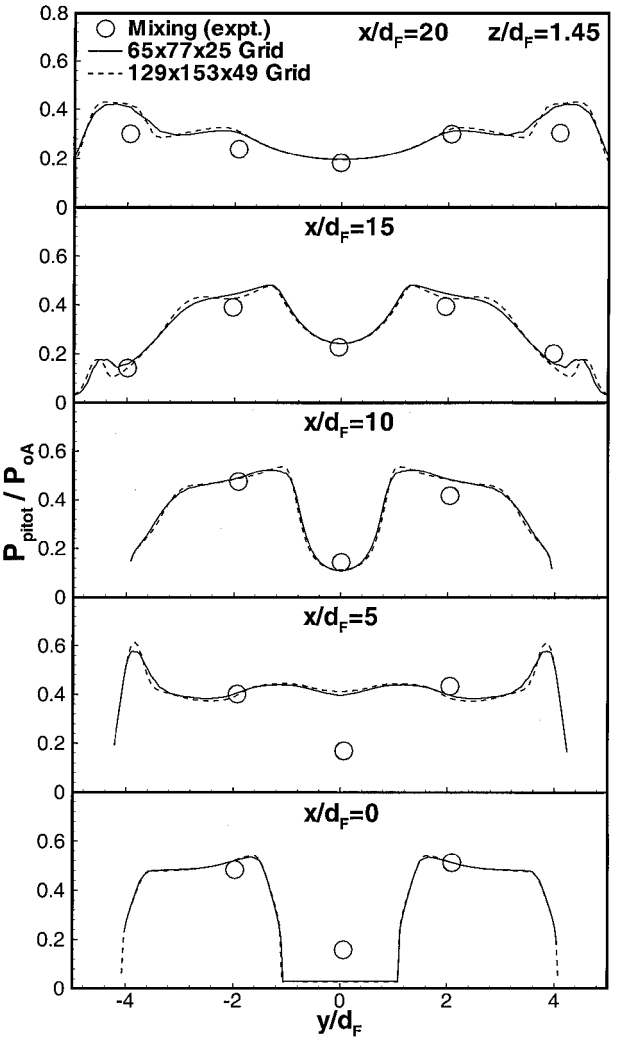

Fig. 7 Normalized pitot pressures at the $z/d_F = 1.45$ midplane for the mixing case with comparison to experimental data of Ref. 10.

located on both figures. The characteristics evidenced are a result of the complex interactions between the recirculation-stabilized flame and different oblique shock systems generated through shear layer displacement effects. As shown in Figs. 10a and 10b, a key feature of the combusting flowfield is the development of a hot, nominally toroidal recirculation zone behind the bluff body (A). The recirculation region is deflected outward into the inviscid wind-tunnel fluid as a result of volumetric expansion caused by heat release and the effects of shock impingement on the recirculation zone. The initial displacement effect creates a shock wave (B) that is nominally conical in shape. This shock wave impinges upon the tunnel walls, creating a large region of three-dimensional, separated fluid, especially evident in the juncture between the side and top walls of the tunnel (C). The displacement effect of this region of separated flow creates a separation shock (D), which crosses the original conical shock and impinges upon the recirculation region at (E). This impingement is an example of a shock-free surface interaction, which results in a downward deflection of the free surface angle to maintain pressure equilibrium.

This shock system, combined with the effective area contraction caused by viscous displacement effects and the pressure rise caused by the 10-deg wedge, compresses the inviscid core fluid, raising its temperature slightly and its density more strongly. The shock wave resulting from the wedge deflection (F) is relatively weak, somewhat diffuse, and nonplanar, as much of the compression occurs through the initial shock system [(B) and (D)] and as boundary-layer displacement effects smooth the sharp change in surface angle.

Relief from this compression process takes place at points (G) and (H) through twin expansion fans emanating from the upper surface junctures. The inviscid core fluid expands rapidly, accelerating axially and radially toward the centerline and separating the fluid behind the bluff body into four counter-rotating vortical structures (or lobes) [I] downstream of the rearward stagnation point (with bilateral symmetry, only one such structure is shown). These structures diverge from the x-y center plane and consist of both cold air, unburned fuel, and hot combustion products. This secondary mixing process is driven primarily by axial vorticity augmentation—a particle entering the vortex from the fuel jet completes approximately $\frac{3}{4}$ of a revolution about the vortex core before exiting the domain. The rapid influx of cold air, combined with induced high strain rates in the neck region downstream of the rearward stagnation point, limits the flame development to the recirculation zone. However, the relief from the strong expansion afforded by the twin reattachment shocks and the presence of some unburned fuel in the vortex core can allow a reignition process further downstream, an effect seen in some of the experimental results. Overall, the structure of the flame shares some commonality with that evidenced in experimental results for axisymmetric bluff-body stabilized flames[30–33] in that near extinguishment in the neck region is followed by a jetlike flame development downstream. Differences in the structure of the jetlike flame relate primarily to the nonuniform pressure field, which precludes the development of axisymmetric features.

Streamline Structure: Reacting Case

Insights into the fuel-air mixing process are provided through three-dimensional stream traces shown in Fig. 11a. Near the

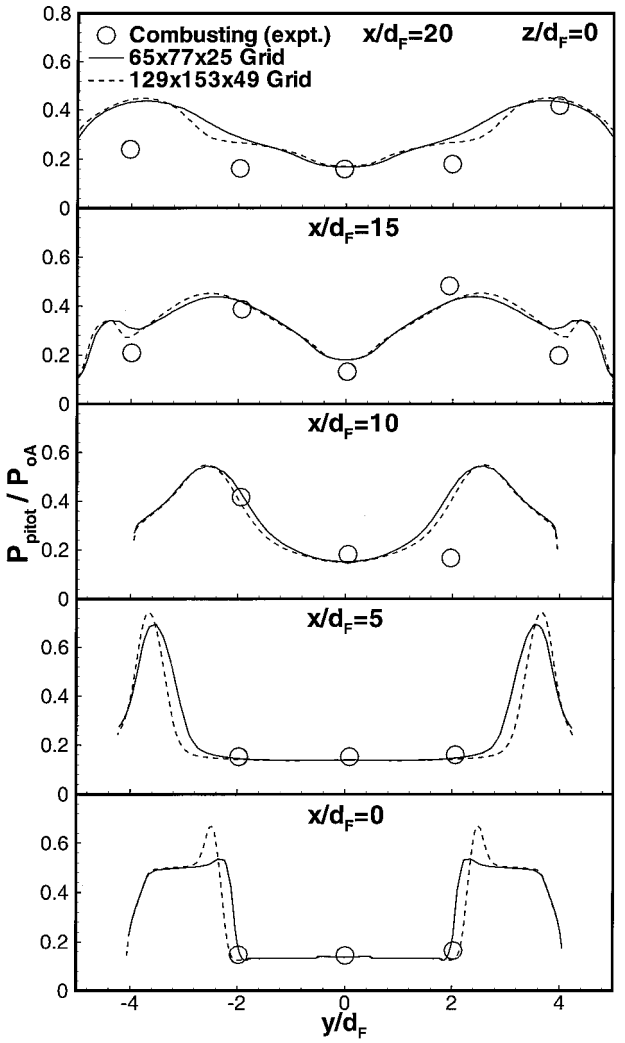

Fig. 8 Normalized pitot pressures at the $z/d_F = 0$ center plane for the combusting case with comparison to experimental data of Ref. 10.

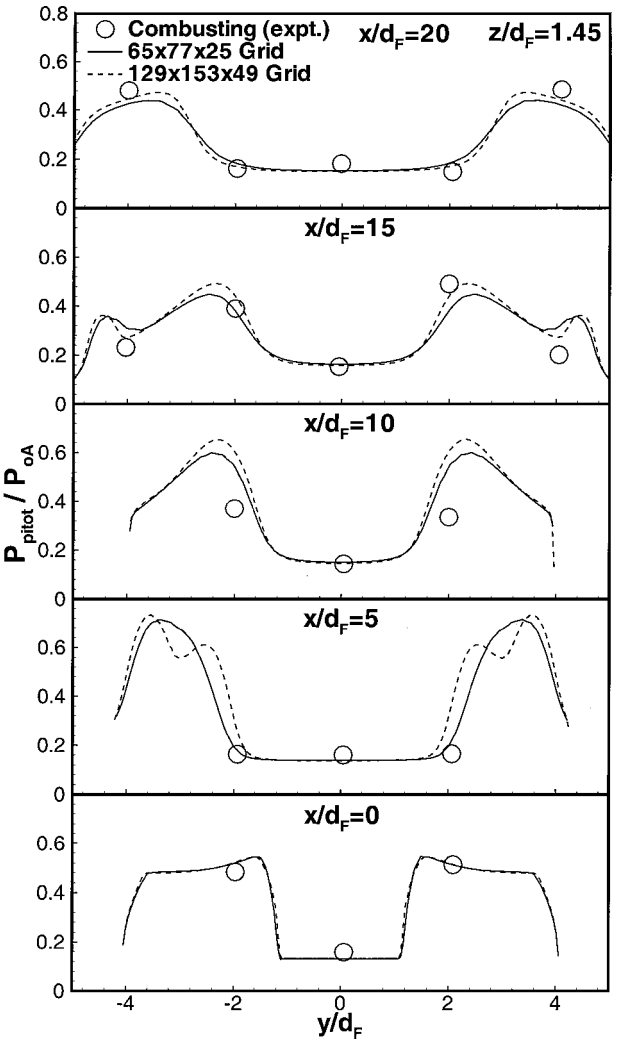

Fig. 9 Normalized pitot pressures at the $z/d_F = 1.45$ midplane for the combusting case with comparison to experimental data of Ref. 10.

bluff-body face the streamline patterns are similar to that of coflow-dominated, bluff-body stabilized flames. The fuel jet completely stagnates (J), with fluid nearest the x-y center plane entrained strongly into a tight toroidal vortex, where it mixes with low-momentum air entrained from the fuel tube boundary layer. After spiraling through the recirculation zone, this fluid is entrained into the outer edge of the axial vortex mentioned earlier (K) before exiting the domain. Mixing is much less rapid for fuel-jet fluid nearer the x-z center plane. This fluid is forced backward toward the bluff-body face then rapidly exits. Little near-wall fluid from the upper surface of the fuel-tube is entrained into the vortex, except near the x-y center plane, where a tight mixing process is evident (L). This location coincides with the impingement point of the separation shock described earlier, which induces a rapid downward change in the shear-layer deflection angle and thus facilitates the entrainment of low-momentum wind-tunnel fluid into the vortex core. The division of the recirculation zone into outer and inner toroidal vortices, as in axisymmetric bluff-body flames, is not pronounced—in particular, the fuel-rich vortex often noted cannot be discerned although a definite air-rich structure is evident. PLIF imaging results from Ref. 28 provide additional support for the presence of significant fuel-jet stagnation, at least in an instantaneous sense.

Reactive Scalar and Flame-Stabilization Trends

Figure 11c shows that the formation of the ignition precursor HO_2 begins just downstream of the bluff-body face. The generation of HO_2 is sustained primarily through the recirculation of hot products back toward the bluff body. Yoon et al.[8] argue that flame stabilization should occur along the stoichiometric contour, where the turbulent flame speed is balanced by the local fluid velocity. Given the three-dimensional structure of the flame, this balance is likely to be first achieved within the tightly wrapped vortex core located approximately at the separation-shock impingement point. Hydroxyl radical (OH) generation occurs downstream of this point, with the band of peak OH (representing the flame front itself) closely following the stream surface that separates the outer portion of the recirculation zone from the inviscid core flow (M). This stream surface also coincides with the stoichiometric contour. Peak temperatures of around 2000 K are observed in the vicinity of the peak OH band [(N), Fig. 10b]. The temperature decreases rapidly further downstream because of the rapid influx of cold air mentioned earlier, and the bluff-body face itself is rather cool (approximately 700 K). The process of flame stabilization in this flow appears to be a synergistic balance between inviscid gas-dynamic processes and dissipative/reactive processes. Impinging shock waves on the recirculation zone result in intense mixing at near stoichiometric conditions near the x-y center plane—the resulting long particle residence times, higher fluid densities, and higher temperatures all promote flame stabilization. The displacement of the hot recirculation zone out into the inviscid core flow actually generates the shock system that helps stabilize the flame—a self-sustaining mechanism that may be somewhat independent of whether additional compression as provided through the 10-deg wedges is present.

Flow Structure: Nonreacting Case

As indicated in Figs. 10 and 11, the nonreacting flow differs significantly from the reactive flow. In contrast to the reactive case, the recirculation zone is not displaced into the tunnel core flow, and no shock wave is induced. Rather, the tunnel fluid expands around the bluff body, producing a toroidal recirculation zone that is nearly

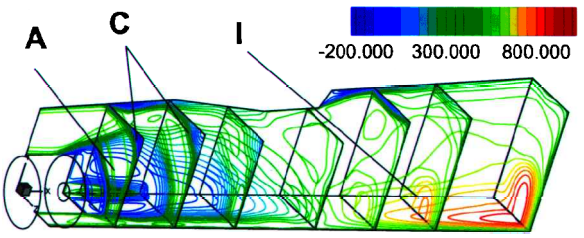

a) Axial velocity (m/s) (reacting)

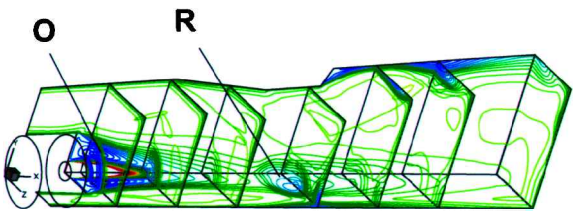

d) Axial velocity (m/s) (nonreacting)

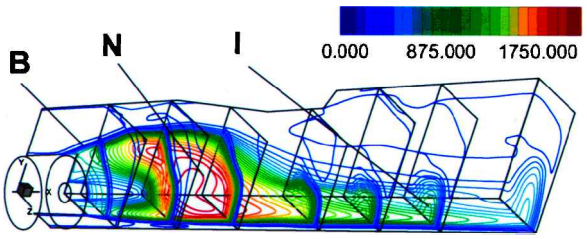

b) Temperature (deg K) (reacting)

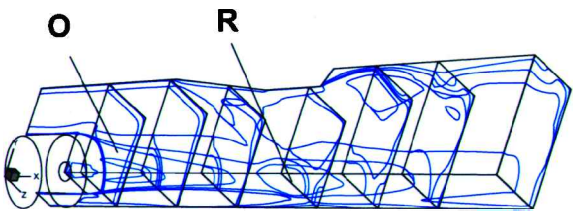

e) Temperature (deg K) (nonreacting)

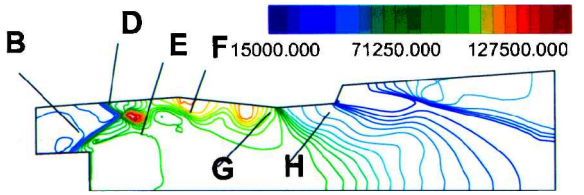

c) Pressure (Pa) (reacting, *x*-*y* centerplane)

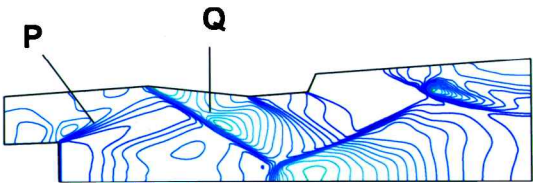

f) Pressure (Pa) (nonreacting, *x*-*y* centerplane)

Fig. 10 Axial velocity, temperature, and pressure for the combusting case (a, b, and c, respectively) and the mixing case (d, e, and f, respectively).

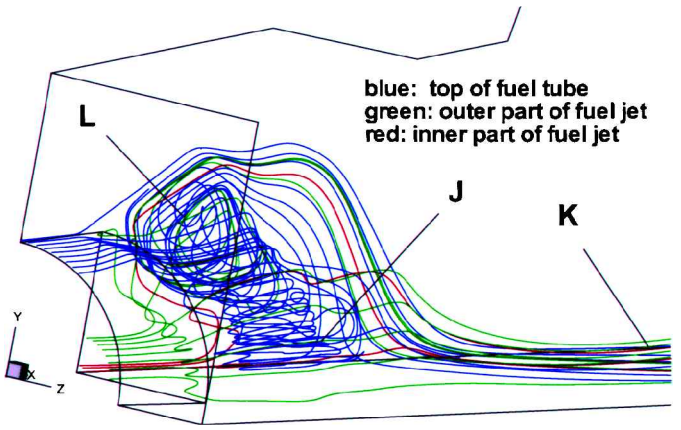

a) Streamtraces (reacting)

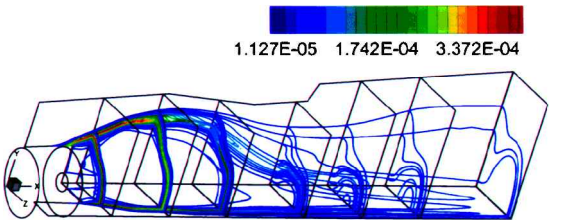

c) HO_2 mass fraction (reacting)

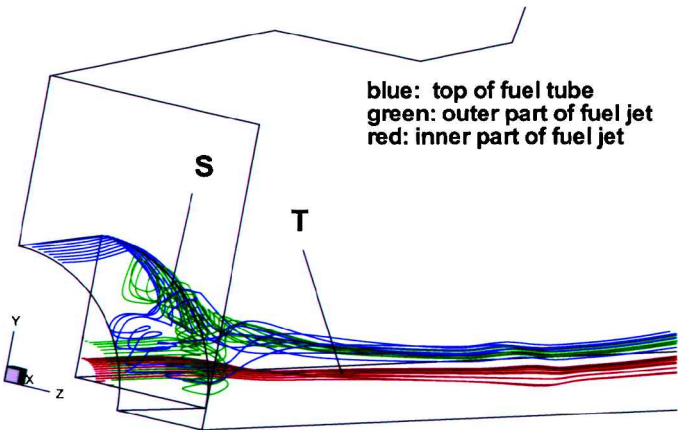

b) Streamtraces (nonreacting)

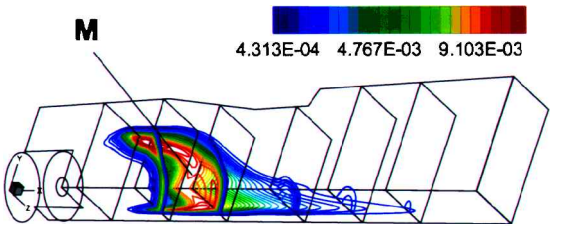

d) OH mass fraction (reacting)

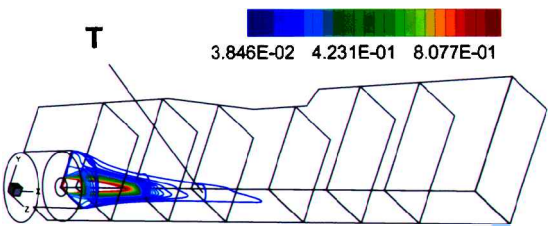

e) H_2 mass fraction (nonreacting)

Fig. 11 Streamlines for a) the combusting case and b) the mixing case, along with HO_2 and hydroxyl mass fractions for the combusting case (c and d, respectively) and fuel mass fraction for the mixing case (e).

axisymmetric in structure (O) (see Fig. 10d). A three-dimensional Prandtl–Meyer wave is generated because of the deflection of the wind-tunnel fluid (P). This wave does not significantly influence the boundary-layer development on the top and side walls. The upper-wall boundary layer, in particular, does not separate until downstream of the end of the 10-deg wedge, and the resulting effects of viscous-layer displacement on the inviscid core flow are minor, compared with the reactive case. The shock wave induced by the wedge (Q) is much stronger, as the precompression induced in the reactive case by multiple shock/viscous-layer interactions is completely absent. This planar shock wave (and its mirror) interact with the low-momentum fluid behind the bluff body, creating a pocket of low-speed flow oriented along the centerline (R). Fluid within this region primarily originates from the inner part of the boundary layer developing on the top of the fuel tube. The transmitted shock emanating from the wedge on the lower surface (included via symmetry boundary conditions) impinges on the top wall aft of the wedge, creating a large recirculation region.

In common with the reactive case, the streamline structure shown in Fig. 11b reveals a nominally toroidal, fuel-lean recirculation zone behind the bluff body. Cold near-wall air is again preferentially entrained into the vortical structure from the portions of the fuel tube nearest the x-y center plane, where it mixes with hydrogen entrained from the outer portion of the fuel tube (S). A coherent fuel-rich vortex near the bluff body is again not easily discernible from the streamlines. In contrast to the reactive flow, fluid emanating from the inner part of the fuel tube penetrates the zone without being entrained into the toroidal structure (T). This behavior is caused by the higher momentum flux of the supersonic hydrogen jet and is consistent with previous characterizations[32,33] of fuel-jet dominated, bluff-body flows. This fluid diverges around the centerline separation zone and is entrained into the outer edges of the developing axial vortices, initiated through baroclinic torque mechanisms downstream of the shock interaction. The splitting of the low-momentum fluid into distinct lobes diverging from the x-y center plane is not as pronounced as in the reactive case.

Conclusions

The results presented in this paper represent an initial attempt to simulate some of the complex-flame/shock-wave interaction experiments conducted by Driscoll and coworkers.[10,11] These flowfields are highly three-dimensional, with the initial mixing process representative of that observed in axisymmetric bluff-body flows and the later stages influenced strongly by the development and growth of axial vortices. Comparisons with schlieren imaging, pitot pressure, and static pressure data of Huh and Driscoll[10,11] give confidence in the ability of the numerical model to capture the large-scale features of the interactions. Discrepancies in the data comparisons can be traced to uncertainties in the combustor inflow conditions and to inadequacies in the turbulence model in predicting recirculating flows.

The results also indicate that the computed flame is stabilized because of a synergistic interaction of a shock system created through volumetric expansion effects with the hot recirculation zone itself. Impinging shock waves on the recirculation zone result in intense mixing at near stoichiometric conditions on the outside of the recirculation zone—the resulting long particle residence times, higher fluid densities, and higher temperatures all promote flame stabilization. The displacement of the hot recirculation zone out into the inviscid core flow actually generates the shock system that helps stabilize the flame. This self-sustaining mechanism may be independent of whether or not additional compression as provided through the 10-deg wedges is present. Detailed simulations of experimental configurations without wedges are planned to determine whether this conjecture holds. Because of the complexity of the flowfields, the expense of the three-dimensional calculations and the low static temperatures involved, the Huh and Driscoll database is less attractive as a means of assessing fundamental developments in supersonic turbulent combustion modeling (an original purpose of the experiments). Rather, it is more illustrative of the strong coupling among shock waves, boundary layers, and reactive shear layers that may occur in an actual scramjet combustor and should be employed in the assessment of CFD technology for analyzing such systems.

Acknowledgments

This work was supported in part by the North Carolina Space Grant Consortium and the Air Force Office of Scientific Research (Grant F49620-98-1-0238, monitored by Len Sakell). The authors would like to thank the North Carolina Supercomputer Center for computer time on the Cray T-91D vector supercomputer.

References

[1]Heiser, W. H., and Pratt, D. T., *Hypersonic Airbreathing Propulsion*, AIAA, Washington, DC, 1994, pp. 14–22.

[2]Eklund, D. R., and Stouffer, S. D., "A Numerical and Experimental Study of a Supersonic Combustor Employing Swept Ramp Fuel Injectors," AIAA Paper 94-2819, June 1994.

[3]Baurle, R. A., Alexopoulos, G. A., and Hassan, H. A., "Analysis of Supersonic Combustors with Swept Ramp Injectors," AIAA Paper 95-2413, July 1995.

[4]Baurle, R. A., Alexopoulos, G. A., and Hassan, H. A., "Analysis of Supersonic Combustors with Swept Ramp Injectors," *Journal of Propulsion and Power*, Vol. 13, No. 2, 1997, pp. 327, 328.

[5]Baurle, R. A., Mathur, T., Gruber, M. R., and Jackson, K. R., "A Numerical and Experimental Investigation of a Scramjet Combustor for Hypersonic Missile Applications," AIAA Paper 98-3121, July 1998.

[6]Menter, F. R., "Two-Equation Eddy-Viscosity Turbulence Models for Engineering Applications," *AIAA Journal*, Vol. 32, No. 8, 1994, pp. 1598–1605.

[7]Driscoll, J. F., Huh, H., Yoon, Y., and Donbar, J., "Measured Lengths of Supersonic Hydrogen-Air Jet Flames—Compared to Subsonic Flame Lengths—and Analysis," *Combustion and Flame*, Vol. 107, No. 1–2, 1996, pp. 176–186.

[8]Yoon, Y., Donbar, J., and Driscoll, J. F., "Blowout Stability Limits of a Hydrogen Jet Flame in a Supersonic, Heated, Co-Flowing Air Stream," *Combustion Science and Technology*, Vol. 97, No. 1–3, 1994, pp. 137–156.

[9]Yoon, Y., Donbar, J. M., Huh, H., and Driscoll, J. F., "Measured Supersonic Flame Properties: Heat-Release Patterns, Pressure Losses, Thermal Choking Limits," *Journal of Propulsion and Power*, Vol. 12, No. 4, 1996, pp. 718–723.

[10]Huh, H., and Driscoll, J. F., "Measured Effects of Shock Waves on Supersonic Hydrogen-Air Flames," AIAA Paper 96-3035, July 1996.

[11]Huh, H., and Driscoll, J. F., "Shock-Wave-Enhancement of the Mixing and the Stability Limits of Supersonic Hydrogen-Air Jet Flames," *26th Symposium (International) on Combustion*, Combustion Inst., Pittsburgh, PA, 1996, pp. 2933–2939.

[12]Ratner, A., and Driscoll, J. F., "The Combustion Efficiency of Supersonic Hydrogen-Air Flames," *Proceedings of the 1997 Fall Technical Meeting of the Eastern States Section of the Combustion Institute*, Combustion Inst., Pittsburgh, PA, 1997, pp. 321–324.

[13]Ratner, A., and Driscoll, J. F., "Effects of Shock Waves on Combustion Efficiency on Supersonic Flames," AIAA Paper 98-1058, Jan. 1998.

[14]Marble, F. E., "Gasdynamic Enhancement of Non Premixed Combustion," *25th Symposium (International) on Combustion*, Combustion Inst., Pittsburgh, PA, 1994, pp. 1–12.

[15]Northam, G. B., Greenberg, I., Byington, C. S., and Capriotti, D. P., "Evaluation of Parallel Injector Configurations for Mach 2 Combustion," *Journal of Propulsion and Power*, Vol. 8, No. 2, 1992, pp. 491–499.

[16]Edwards, J. R., "Advanced Implicit Methods for Finite-Rate Hydrogen-Air Combustion Calculations," AIAA Paper 96-3129, July 1996.

[17]McBride, B. J., Gordon, S., and Reno, M. A., "Coefficients for Calculating Thermodynamic and Transport Properties of Individual Species," NASA TM-4513, Oct. 1993.

[18]Frankel, S. H., Drummond, J. P., and Hassan, H. A., "A Hybrid Reynolds Averaged/PDF Closure Model for Supersonic Turbulent Combustion," AIAA Paper 90-1573, June 1990.

[19]Baurle, R. A., Drummond, J. P., and Hassan, H. A., "An Assumed PDF Approach for the Calculation of Supersonic Mixing Layers," AIAA Paper 92-0182, Jan. 1992.

[20]Roy, C. J., "A Computational Study of Turbulent Reacting Flowfields for Scramjet Applications," Ph.D. Dissertation, Dept. of Mechanical and Aerospace Engineering, North Carolina State Univ., Raleigh, NC, Dec. 1998.

[21]Roy, C. J., and Edwards, J. R., "Bluff-Body Stabilized Flame Calculations with the k-ς Two-Equation Turbulence Model," AIAA Paper 98-0252, Jan. 1998.

[22]Balakrishnan, G., Smooke, M. D., and Williams, F. A., "A Numerical Investigation of Extinction and Ignition Limits in Laminar Nonpremixed Counterflowing Hydrogen-Air Streams for both Elementary and Reduced Chemistry," *Combustion and Flame*, Vol. 102, No. 3, 1995, pp. 329–340.

[23]Edwards, J. R., "A Low-Diffusion Flux-Splitting Scheme for Navier–Stokes Calculations," *Computers and Fluids*, Vol. 26, No. 6, 1997, pp. 635–659.

[24] Saad, Y., and Schultz, M. H., "GMRES: A Generalized Minimum Residual Algorithm for Solving Nonsymmetric Linear Systems," *SIAM Journal of Scientific and Statistical Computation*, Vol. 7, No. 3, 1986, pp. 856–879.

[25] Roy, C. J., and Edwards, J. R., "Bluff-Body Stabilization Effects in Supersonic Turbulent Combustion," *Proceedings of the 1997 Fall Technical Meeting of the Eastern States Section of the Combustion Institute*, 1997, pp. 115–118.

[26] McDaniel, K. S., and Edwards, J. R., "Simulation of Thermal Choking in a Model Scramjet Combustor," AIAA Paper 99-3411, June 1999.

[27] Edwards, J. R., and Roy, C. J., "Preconditioned Multigrid Methods for Two-Dimensional Combustion Calculations at All Speeds," *AIAA Journal*, Vol. 36, No. 2, 1998, pp. 185–192.

[28] Bryant, R. A., Ratner, A., and Driscoll, J. F., "Using PLIF Determined Flame Structure to Analyze Supersonic Combustion Efficiencies," AIAA Paper 99-0445, Jan. 1999.

[29] Dally, B. B., Fletcher, D. F., and Masri, A. R., "Flow and Mixing Fields of Turbulent Bluff-Body Jets and Flames," *Combustion Theory and Modeling*, Vol. 2, No. 2, 1998, pp. 193–219.

[30] Schefer, R. W., Namazian, M., and Kelly, J., "Velocity Measurements in a Turbulent Non-premixed Bluff-Body Stabilized Flame," *Combustion Science and Technology*, Vol. 56, No. 4–6, 1987, pp. 101–138.

[31] Roquemore, W. M., Bradley, R. P., Stutrud, J. S., Reeves, C. M., Britton, R. L., Sandhu, S. S., and Archer, R. S., "Influence of the Vortex Shedding Process on a Bluff-Body Diffusion Flame," AIAA Paper 83-0335, Jan. 1983.

[32] Masri, A. R., Dally, B. B., Barlow, R. S., and Carter, C. D., "The Structure of the Recirculation Zone of a Bluff-Body Combustor," *25th Symposium (International) on Combustion*, Combustion Inst., Pittsburgh, PA, 1994, pp. 1301–1308.

[33] Correa, S. M., and Pope, S. B., "Comparison of a Monte Carlo PDF/Finite Volume Mean Flow Model with Bluff-Body Raman Data," *24th Symposium (International) on Combustion*, Combustion Inst., Pittsburgh, PA, 1992, pp. 279–285.

P. Givi
Associate Editor

Color reproductions courtesy of Sandia National Laboratories.